Electrochimica Acta 497 (2024) 144550

Contents lists available at ScienceDirect

Electrochimica Acta

journal homepage: www.journals.elsevier.com/electrochimica-acta

Elucidating the mechanisms of microbubble formation in intracardiac pulsed field ablation

Samo Mahnič-Kalamiza [a], Damijan Miklavčič [a], Peter Lombergar [a], Blaž Mikuž [b], Lars M. Mattison [c], Daniel C. Sigg [c], Bor Kos [a,*]

[a] University of Ljubljana, Faculty of Electrical Engineering, Tržaška c. 25, SI-1000 Ljubljana, Slovenia
[b] Jožef Stefan Institute, Reactor Engineering Division, Jamova 39, 1000 Ljubljana, Slovenia
[c] Medtronic, 8200 Coral Sea St NE, Mounds View, MN 55112, USA

ARTICLE INFO

Keywords:
Pulsed field ablation
Gas release
Electrochemistry
Joule heating
Water phase transition

ABSTRACT

Delivery of electrical energy for sensing or therapeutic purposes often involves electrochemical phenomena at the electrode-electrolyte solution interface. Release of gaseous bubbles that accompanies delivery of pulsed electric fields to tissues in applications such as electrochemotherapy of tumours and irreversible electroporation or pulsed field ablation in cardiac electrophysiology needs to be understood and characterized. We present an *in vitro* study using pulsed field delivery into saline, employing multiple different treatment protocols, two electrode geometries (pair of needles and a modified RF catheter), and two imaging systems to elucidate the complex relationship between the electrical treatment protocol, temperature changes at and around the electrodes, and gas release due to pulse delivery. Our primary objective was to identify the key parameters responsible for bubble formation and to highlight the importance of the treatment parameters and their interplay – ranging from the temperature to appropriate choice of electrode geometry, and, most importantly, to the choice of the treatment protocol. We found that bubbles originating from electrochemical reactions are more prevalent in monophasic pulsing protocols, whereas in high frequency biphasic pulsing protocols the bubbles are mainly caused by boiling of the medium. Degassing of liquid due to lower solubility of gasses at elevated temperatures does seems to play a role, though a minor one. We also observed that bubbles caused by boiling collapse very rapidly, whereas electrochemically produced bubbles or those produced through degassing appear to have longer lifetimes. Therefore, the treatment protocols most suited to minimizing gas release are biphasic trains of short (μs) pulses with a significant inter-pulse delay (i.e. low duty cycle) to prevent excessive heating. Moreover, electrodes must be designed to avoid high local current densities. Our findings have broad implications extending from lab-on-a-chip cell electroporation devices to intracorporeal pulsed field applications in the cardiovascular system, particularly pulsed field ablation procedures.

1. Introduction

Electroporation is a phenomenon and treatment modality whereby short, high-intensity electrical impulses are delivered to cells or tissues with the purpose of altering the cell membrane to introduce/extract molecules to/out of cells, or to kill them. Applications range from drug delivery to single cells in suspensions [1] or lab-on-a-chip applications [2], to cardiac tissue ablation, known as pulsed field ablation (PFA) [3], and structures deeply embedded into organs (e.g., tumours [4]).

Charge transfer between the electrodes and the cell suspension or tissue is often unavoidably associated with the application of electrical pulses used to achieve electroporation, leading to redox reactions at the electrodes. If the duration of a single pulse phase is sufficient, it can completely charge up the double layer capacitance, leading in continuation to charge transfer between the medium and the electrodes, resulting in faradaic reactions that lead to water electrolysis. Products of these reactions are not only ions, but also gasses; namely, hydrogen, oxygen, and chlorine (for pulse delivery to an aqueous solution of NaCl). Energy delivery can be intense and cause a considerable rise in temperature, reaching the boiling point of water, leading to release of water vapour.

Release of gaseous bubbles during intracorporeal application of

* Corresponding author.
E-mail address: bor.kos@fe.uni-lj.si (B. Kos).

https://doi.org/10.1016/j.electacta.2024.144550
Received 15 January 2024; Received in revised form 15 May 2024; Accepted 6 June 2024
Available online 7 June 2024

electroporation was previously observed and reported in biomedical applications such as electrochemotherapy [5–7] and irreversible electroporation [8,9], raising treatment safety concerns for PFA when used for treatment of cardiac arrhythmias [3,10–12]. With rapidly growing use and adoption of PFA, this issue has to be considered since intracardial DC discharges can lead to gas release with associated risk of microemboli [13,14]. Also, as demonstrated in RFA (radiofrequency ablation), heating can cause gas bubble and coagulum formation originating at the catheter-blood interface and their release into the bloodstream and into organs such as kidneys, lungs, or the brain, potentially resulting in coronary occlusion, stroke, or silent cerebral events [15–17].

We can identify three possible mechanisms of bubble formation and growth: a.) release of gas due to lower gas solubility at elevated temperatures of the medium (we refer to this as *degassing*), b.) release of gas as water vapour (boiling), and c.) release of gas as a product of hydrolysis (water electrolysis at the electrodes) and oxidation of chlorine ions. The first two origins are thermal in nature, while the third is electrochemical.

Available clinical data on PFA shows comparable rates of silent cerebral lesions and silent cerebral events in recent trials to those reported for thermal-based ablation technologies [18,19]. Nevertheless, since the release of gas bubbles could potentially result in an embolism, it should be kept at a minimum whilst maintaining sufficient treatment intensity for a therapeutic effect. Thus, our understanding of the mechanisms governing the bubble origin is essential.

We performed an *in vitro* study using pulsed field delivery into saline, employing multiple different treatment protocols, two electrode geometries (parallel needles and a modified RF catheter [20]), and two imaging systems to elucidate the complex relationship between treatment protocols, thermal relations at the electrodes, and gas release concomitant to pulse delivery and bubble behaviour after delivery. We used two imaging systems since the "slow", microscopic camera is more suited to capturing the visuals of bubble evolution using the parallel needle geometry where the electrodes are spaced further apart, while the high-speed camera is more suitable for capturing the visuals of bubble evolution using the RF catheter and for enabling a finer temporal resolution conducive to study of microbubble origins. We performed numerical simulations to study thermal relations in the vicinity of the electrodes to examine boiling of the medium. We also used elevated temperatures of the saline in our experiments to see whether the lower solubility of gasses at elevated temperatures will lead to higher numbers and volumes of bubbles (i.e., due to an increased rate of degassing of liquid or reduced ability of water to dissolve electrolytic products). Finally, we performed experiments with an ultrasound-based bubble loop flow setup to determine the number and volume of bubbles which persist in the liquid media and can detach from the catheter.

2. Materials and methods

2.1. Pulse protocols

We used 9 different pulse protocols chosen based on literature, both monophasic and biphasic, with an array of pulse lengths and varying inter-pulse delays, thus varying the "duty cycle" of the pulse train and the power of electrical energy delivery. All the protocols are given in

Table 1
Pulse parameters used throughout the study. The pulses are illustrated in Fig. 1A.

Protocol No.	*Protocol name / shorthand*	*Positive phase duration [μs]*	*Pause between phases [μs]*	*Negative phase duration [μs]*	*Pause between pulses [μs]*	*Number of pulses in burst (p_N)*	*Number of bursts (G_N)*	*Burst repetition frequency [s^{-1}]*	*Duration of one pulse train [ms]*	*References*	*Used in 30 fps microsc. cam. exp.*	*Used in high-speed camera exp.*
1	Exponentially decaying pulse, τ = 6 ms *"exponential"*	—	—	—	—	1	1	—	—	[12]	Y	N
2	Monophasic 100 μs at 1 s^{-1} *"100–1e6"*	100	0	0	—	1	90 / 30	1	0.1	[21]	Y	Y
3	5 kHz monophasic 100 μs – anode on tip *"100–100″*	100	—	—	100	8	1	—	1.5	[22]	N	Y
4	5 kHz monophasic 100 μs – reversed polarity, cathode on tip *"reversed 100–100″*	100	—	—	100	8	1	—	1.5	[22]	N	Y
5	High duty factor biphasic *"2–2–2–2″*	2	2	2	2	216	1	—	1.73	[23]	N	Y
6	Low duty factor biphasic *"2–2–2–500″*	2	2	2	500	216	1	—	109	Original	N	Y
7	Low duty factor biphasic – longer pulses *"5–5–5–500″*	5	5	5	500	80	1	—	41.2	[24]	Y	Y
8	Rectangular biphasic *"3–0–3–0″*	3	0.4	3	0.4	333	10	2	2.3	[25]	Y	N
9	Low duty cycle biphasic – longer inter-pulse delay *"1–1–1–1000″*	1	1	1	1000	999	10	0.99	1002	[26]	Y	N

Table 1, with Fig. 1a provided for easier understanding of used pulse parameters.

2.2. Acquiring video evidence of bubble formation in saline

2.2.1. Experiments using a 30 frame-per-second (fps) microscopic camera

The initial study used a standard 30 fps microscopic camera (ShowRange, SRM-800X USB Digital Microscope, Shanghai, PRC). Pulses were applied in 0.9 % saline (B Braun, Melsungen, Germany) at room temperature using a prototype pulse generator (University of Ljubljana, Faculty of Electrical Engineering, Slovenia) [27]. Two needle electrodes made of platinum (99.99 % Pt, cat. no. PT005155, Goodfellow Cambridge) of 1 mm diameter and 60 mm in length were submerged 5 mm deep into the solution filling a 100 mL size beaker up to 80 mL solution volume. The electrodes were 5 mm apart, measured centre-to-centre. Videos were captured through the glass side of the beaker at an appropriate distance and zoom level. Five different pulse protocols were used for this study, the parameters are given in Table 1. Pulse protocols used for this study were the five listed in Table 1, entries 1–2 and 7–9. The temperature was closely monitored with an optical sensor in proximity (within 1 mm) of the electrode surface using an OpSens optical thermometer PSC-D-N—N using a single module PSR-G1–10–100ST and an OTG-MPK5 fibre optic sensor (OpSens Solutions Inc, Canada).

Next, we performed experiments at different solution temperatures either lower (10 °C), or higher than room temperature (40, 60, or 70 °C), to test for the impact of lower gas solubility at higher temperatures on gas evolution. We employed protocols 100–1e6 (no. 2, Table 1) and 5–5–5–500 (no. 7, Table 1) to compare a monophasic with a biphasic protocol [24]. Cooling of the solution in an ice bath or heating of the solution with a hot plate was combined with magnetic stirring, achieved using a standard laboratory magnetic stirrer & hot plate or an ice pack. The temperature was controlled using the same optical thermometer as described, however, the sensor was at least 3 cm away from the electrodes in the solution.

During pulse deliveries, voltage and current were measured using a HDO6104A-MS oscilloscope with HVD3206A differential voltage probe and CP31A current probe (all from Teledyne LeCroy, Chestnut Ridge, NY, USA). The temperatures at which recordings were performed are not the same across experiments for practical reasons and difficulties in maintaining a constant temperature using a hot plate or ice bath. We did however match the electric current across different temperatures by adjusting the voltage to keep the current amplitude constant (conductivity is temperature-dependant) for all experiments, since electrolysis is proportional to the transferred charge.

2.2.2. Experiments using a high-speed camera

Experiments were performed in the THELMA lab of Reactor Engineering Division at Jožef Stefan Institute using a setup consisting of a Phantom v1212 camera (Vision Research, Wayne, NJ, USA) with a Laowa 25 mm f/2.8 2.5–5x Ultra Macro lens (Venus Optics, Hefei, China) at 3:1 magnification. Video was captured at 10 kfps and recording was triggered by a TTL pulse from the measurement oscilloscope to synchronize the recording with the pulse output. Additional illumination was provided by a LED -illuminated white back panel and an additional flexible 6 W LED light source Kern OZB-A4515 (KERN & SOHN GmbH, Balingen-Frommern, Germany). Exposure duration was always 98 µs.

Experiments were performed with a set of parallel needle electrodes as previously described and a modified ContactR™ catheter with a 5-mm tip (Medtronic, Minneapolis, MN, USA). The catheter was modified to allow bipolar delivery-between the catheter tip and the three ring electrodes included on the catheter for measurement of bipolar intracardiac electrograms. The experimental setup is shown in Fig. 1b. The catheter was submerged in a 200 mL beaker filled to the nominal capacity with 0.45 % saline (diluted physiological saline with deionized water). The concentration of salt in the catheter experiments was used to mimic the conductivity of blood, so that currents and surface current density are closer to what would be seen in actual treatment. The

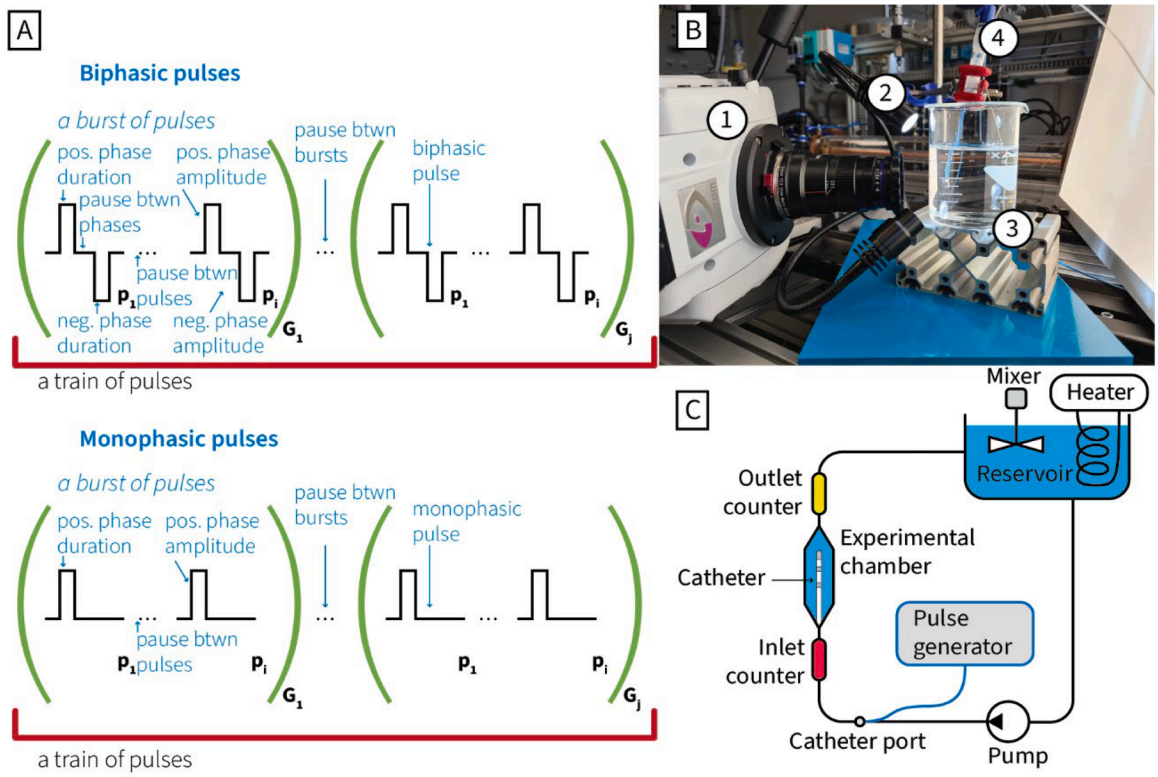

Fig. 1. Methods illustrated. a) Schematic nomenclature illustrating pulse waveforms listed in Table 1. b) Photo of the experimental setup with high-speed camera. (1) Phantom v1212 camera with Ultra Macro lens, (2) Light source, (3) Beaker with saline, (4) Holder with catheter. c) Schematic illustration of the bubble loop setup.

catheter was not centred in the beaker but brought closer to the camera's lens into its working distance. Where bubble volume was determined from the high-speed camera, this was done by calibrating the scale with known catheter dimensions and measuring the bubble diameter using ImageJ [28].

2.3. Experiments with a bubble counter

To determine the number and volume of bubbles which persist in the liquid media, we performed experiments using a bubble counter. A schematic of the setup is shown in Fig. 1C. The setup consisted of a flow-through cylindrical chamber with 40 mm inner diameter and 100 mm length, which has a total working volume of 125 ml. The total medium volume available for electric current flow was therefore comparable to the one used in the high-speed camera experiments. The bubble loop featured a pump (Bio-Console™ 560 with BPX-80 Bio-Pump® centrifugal pump, both from Medtronic, Minneapolis, MN, USA) with 1 l/min flow, and a bubble counter with two ultrasonic sensors (BCF300, Gampt mbH, Merseburg, Germany), where one was positioned before the treatment chamber, to measure bubbles flowing into the chamber and the second sensor immediately after the chamber to determine how many bubbles were flowing out. The experimental chamber and sensor after the chamber were positioned vertically, to prevent bubbles being trapped on the path from the catheter to the detector. Temperature control of the medium in the entire bubble loop was maintained with a thermal bath filled to capacity of 4.5 L (Polystat, Cole-Parmer, Vernon Hills, IL, USA) at 23 °C for the room temperature and 60 °C for the elevated temperature.

2.4. Electric field and current distribution, heat generation and dissipation numerical model

An axisymmetric 2-D numerical model of the bipolar ablation catheter immersed in saline was created in COMSOL Multiphysics (Version 6.1, COMSOL AB, Stockholm Sweden). The axis of symmetry was along the catheter axis. To model temperature increase during pulse application, the continuity equation for charge conservation and the heat equation for energy conservation were coupled and solved. Heating of the saline solution due to pulse application was modelled with the "duty cycle" approach [29]– i.e. constant voltage boundary condition was prescribed at the electrodes and the joule heating source in the heat equation was multiplied with the duty factor (duration/period) of each pulse protocol. This approach ensures equal amounts of total energy (E) delivered to the saline solution as in the experiments, without modelling each individual electrical pulse. Boiling of the solution was included with a simple model, which applied a Heaviside phase transition function for saline temperatures between 100 and 110 °C to account for the latent heat of vaporization. For the gas phase of saline, thermal conductivity and capacity of water vapour were used and the electrical conductivity of 0.45% saline at 100 °C (0.84 S/m at 25 °C, with temperature dependence calculated from [30]; for full table see ST2) was reduced by 66 % to account for the maximum void fraction of close random packing spherical voids due to vapour formation [31]. The actual bubble formation was not included in the model, i.e., we did not

Table 2
Experimental conditions and results. Table shows the applied voltages (**Voltage**) and water bath temperature (**Temp**), measured average applied voltage (**U avg**) and current (**I avg**), total energy (**Energy**), calculated volume of steam (gas phase of saline) in the model at the end of the pulse train (V_{H2Ogas})*, the moment at which bubbles can be first observed in the model (t_{sim})**, the moment when bubbles attributed to boiling can be first observed on high-speed camera (t_{video}), and finally the computed maximum volume of degassed air due to reduced solubility of air's constituent molecules in the saline (V_{degass}).

Pulse Protocol	Temp [°C]	Voltage [V]	U avg [V]	I avg [A]	Energy [J]	V_{H20gas} [µl]	t_{sim} [ms]	t_{video} [ms]	V_{degass} [µl]
3	26.4	200	190	2.49	0.38	0.00	0		0.02
3	26.4	400	380	5.09	1.54	0.07	0		0.07
3	26.4	500	473	6.41	2.42	1.77	1	1	0.10
3	26.4	600	564	7.76	3.48	7.29	0.7	0.8	0.15
3	56.5	200	187	3.38	0.50	0.00	0		0.01
3	54.5	300	279	4.95	1.10	0.72	1.2	1	0.02
3	52	400	371	6.48	1.91	4.79	0.7	0.6	0.03
3	50.5	500	464	7.67	2.84	16.34	0.5	0.4	0.05
3	49	550	512	8.09	3.30	24.91	0.4	0.3	0.07
4	26.4	600	564	7.80	3.51	7.32	0.7	0.8	0.15
4	46	550	511	8.35	3.40	19.92	0.5	0.3	0.07
5	26.5	400	372	5.12	1.59	0.06	0.4	0.4	0.07
5	26.5	500	463	6.45	2.49	1.73	0.6	0.6	0.11
5	26.3	600	554	7.79	3.60	7.64	0.8	1	0.15
5	26.4	700	645	9.12	4.83	20.11	1.2		0.20
5	26.4	800	734	10.37	6.24	41.34	0		0.26
5	75	300	268	6.44	1.40	7.29	0.6	0.7	0.00
5	71	400	356	8.10	2.36	21.71	0.4	0.4	0.00
6	26.4	400	376	5.20	1.64	0.00	0		0.07
6	26.4	500	467	6.44	2.52	0.00	0		0.11
6	26.4	600	560	7.78	3.64	0.00	0		0.15
6	26.4	700	650	9.15	4.90	0.00	0		0.21
6	26.4	800	739	10.54	6.41	0.00	0		0.27
6	26.4	900	829	11.99	8.28	0.64	102.4		0.33
6	26.4	1000	917	13.43	10.25	12.88	74.8	103	0.41
6	69	600	529	12.19	5.28	34.62	44.5	80	0.01
7	26.4	500	461	6.41	2.33	0.00	0		0.10
7	26.4	700	644	9.16	4.63	0.00	0		0.19
7	26.4	900	822	12.00	7.78	10.84	25.8	35	0.30
7	26.4	1000	908	13.44	9.63	36.59	19	24	0.37
7	63.5	600	533	11.28	4.71	29.41	15	19	0.03
7	60	600	535	10.88	4.57	19.12	18	24	0.03

* Volume of bubbles is calculated by multiplying the volume of gas phase in model with expansion factor for transition between liquid and gas phase of water (1600 at 1 atm pressure). This volume is overestimating the actual volume of bubbles because it does not account for energy required for bubble expansion during phase change).

** threshold for occurrence of bubbles in the model was determined by dividing the minimal volume of bubbles observable in the videos by the expansion factor.

model the volume expansion during the phase change. The density of the saline was kept constant during the phase change to satisfy mass conservation.

Contrary to most research dealing with boiling of water at the surface of a heated wall [32], in our case, the water is directly heated due to Joule losses, and the metal electrodes are heated indirectly through contact with the medium. The bubble volume (Table 2, $\mathbf{V_{gas}}$) was determined by multiplying the gas phase in the simulation with the volume expansion factor (1600 at 1 atm). To determine the moment at which bubbles were first observed in simulation (Table 2, $\mathbf{t_{sim}}$), a threshold of 0.16 µl was chosen, corresponding to the minimal volume of gas detectable in the high-fps video.

We also calculated the maximum possible volume of degassed air due to the local temperature increase and the resulting drop in air solubility [33]. This was done by integrating air solubility as a function of temperature expressed by the Ostwald coefficient [34] over the entire

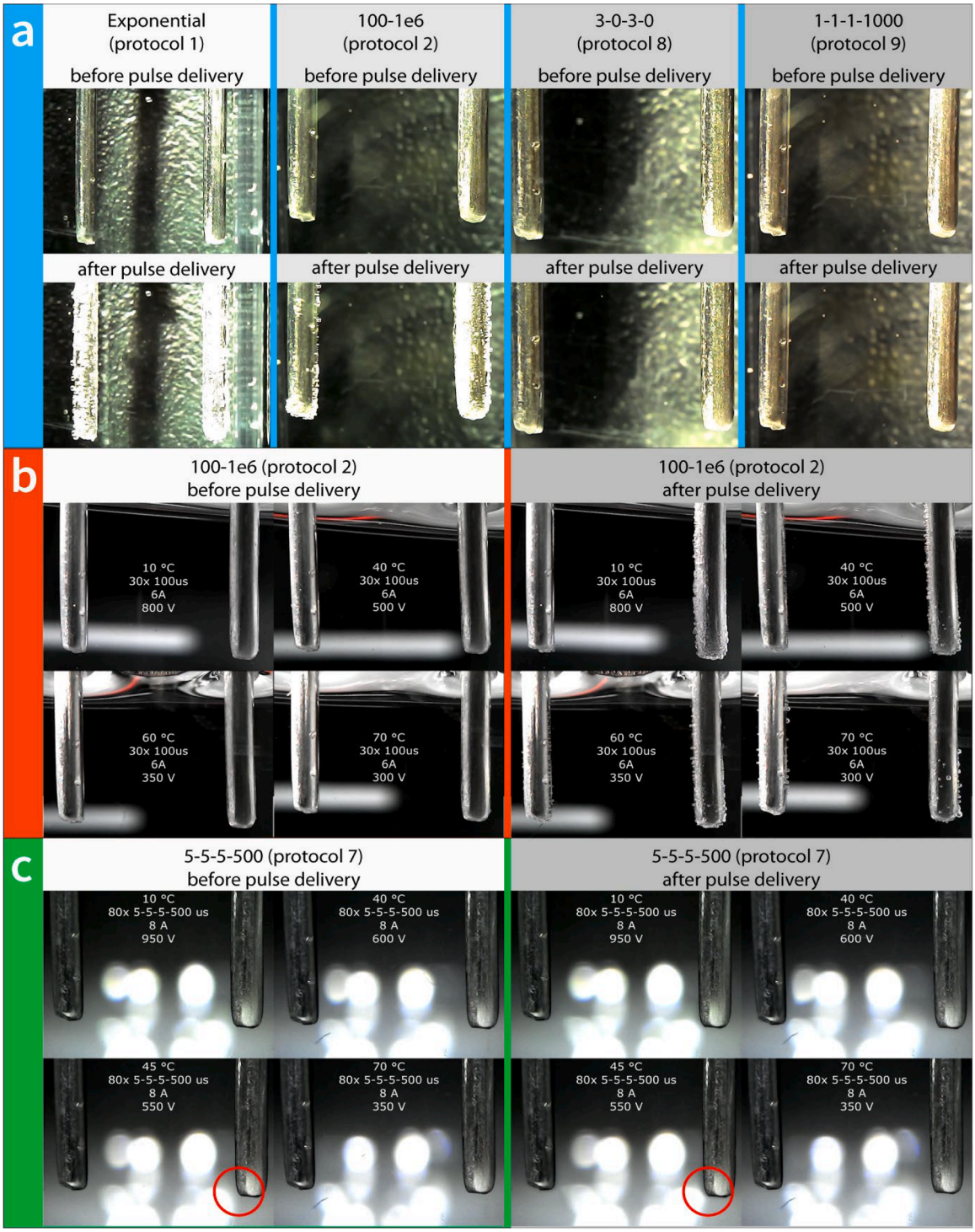

Fig. 2. a. Comparison of bubble release between four different protocols at room temperature. Cathode is on the right (if applicable). b. Stills from the "gas solubility vs. temperature" videos – monophasic pulses, protocol 100–1e6. c. Stills from the "gas solubility vs. temperature" videos – short biphasic pulses, protocol 1–1–1–1000. Red circle highlights an optical distortion at the instance of pulse application.

volume of saline, where we assumed saturation with air at atmospheric pressure.

3. Results and discussion

3.1. Results of the microscopic, 30 fps camera experiments

We refer the reader to the supplementary video material, as the still images (video frames) shown in figures are barely representative of the effects observable on video. Specifically, still images fail to capture the number and volume of the bubbles released using monophasic protocols since most bubbles will immediately separate from the electrode and flow up to the medium surface. These dynamics of bubble growth and detachment are important to mention and briefly discuss at this point. It should be noted that only bubbles that do not detach from the surface of the electrodes have the potential to grow into larger bubbles. It is therefore important how strongly the bubbles are attached to the electrode surface and whether they are in cavities or other surface discontinuities where they can continue to grow substantially before detaching. Sufficiently large bubbles can also coalesce when in proximity into even larger ones, eventually creating favourable conditions for arcing as gas contained within the bubble ionizes and conducts electrical current. This is particularly undesirable and tend to occur at electrode edges where the current density is the highest.

In Fig. 2a, note the difference in released gas volume between the mono- and biphasic pulse delivery (i.e., exponential and 100–1e6 vs. 3–0–3–0 and 1–1–1–1000). There is an obvious difference in the quantity of released gas when contrasting monophasic against the biphasic waveforms. In this set of experiments, there were no observable bubbles formed during biphasic waveform delivery, i.e., none originating in hydrolysis. There were also no significant rises in temperature (see Figure S1 in the Supplement), suggesting that any bubbles (if observed) would be either due to electrolysis or degassing of liquid, but not boiling. As expected, biphasic protocols generate the least amount of gas but most strongly heat up the medium near the electrodes. It would appear thus that the choice of monophasic vs. biphasic delivery is an easy one, however, the reader should beware that in order to achieve the same electroporation effect, short biphasic pulses prove less effective than longer monophasic ones at the same voltage amplitude/field strength, meaning that higher voltages or possibly larger number of pulses need be applied to achieve a comparable effect when biphasic protocols are used [35–38]. There is even a difference in efficacy between biphasic protocols where delivered energy is the same but the protocol is varied in the sense of interphase and interpulse delay, as shown in e.g. [26].

At the outset, we estimated that the degassing of liquid due to temperatures below the boiling point of water can be considered of small importance. For reference, we provide a table (ST1) showing solubility of air in water over a wide range of temperatures [33]. From a human body temperature of 37 °C up to 80 °C, the solubility of air in water (i.e., blood) falls by mere 12 %, which would mean that only a small volume of gas could be degassed as bubbles.

In Fig. 2b (see related video), note the limited impact of temperature on the amount and size of released bubbles for monophasic pulses (protocol 100–1e6). This is in line with the expectation that temperature has a negligible effect on gas release through degassing of dissolved air. In monophasic protocol experiments, there is again more gas released at the cathode than at the anode. If bubbles were not electrochemical in nature, but due to degassing, we would expect comparable volumes of gas irrespective of the polarity.

Experiments at elevated temperature (Fig. 2b and c) have shown little evidence of degassing, but there might be a dependence of electrochemical reaction rate on temperature.

In Fig. 2c, note the impact of a sudden increase in temperature on image distortion (a change in light deflection) in the video (barely detectable on figure) in the proximity of the electrode tips (circled in red), which occurs the moment the pulse train is delivered. The white patches are reflections of the light sources illuminating the beaker from the walls of the beaker and will appear to “move” when the optical properties of the medium change due to heating, resulting in the effect that is noticeable on video near the encircled area. Overall, we did not observe any bubble formation regardless of the initial medium temperature for biphasic protocols.

3.2. Results of the high-speed (10 kfps) camera and the bubble loop experiments

The experiments with the high-speed camera and modified RFA catheter demonstrated temporal dynamics of bubble formation during delivery of the high-rate pulse sequences used in the experiments. All experiments were complemented by numerical simulations to determine spatial and temporal distribution of the temperature. The numerical results are shown in Table 2. Based on the numerical simulations, the highest temperature rise was measured near the leading edge of the first ring electrode, consistent with the highest current density expected near this electrode. This is also the location with the highest electric field strength (Figure S2). This was due to the asymmetrical structure of the electrodes (the tip electrode has a larger surface area than the ring electrodes) and the small distance between the tip and the first ring electrode (3 mm). The heating occurs due to Joule losses in the electrolyte solution, meaning that the temperatures in the medium are always highest, and the metallic electrodes are heated indirectly by the liquid.

Fig. 3 shows a comparison between two different electrode polarities (protocols 100–1e6 and reversed 100–1e6) with resulting differences in electrochemical effects. In the case where the anode was the tip, we observed arcing near the leading edge of the ring electrode (Fig. 3, frame 6). This arcing occurred during the last two pulses of the train. During this period, the model predicted boiling near the electrode edges, and significant shock-wave-induced motion can be seen (Fig. 3, frames 6–8). With reversed polarity, when the cathode is the tip electrode, no arcing was observed, a larger volume of hydrogen gas covers the tip electrode, and the density of bubbles near the ring electrode is lower. This compares well with previous findings of current-controlled catheter ablation [14], where shockwave and voltage breakdown were first described and ultimately led to the abandonment of DC ablation in cardiac electrophysiology in favour of the slower, but safer, RF ablation. Bardy et al. [14] observed voltage breakdown after 300–400 μs with an applied current of approximately 8 A. This is a shorter duration than in our experiment, however, they used a long single pulse instead of the 100 μs pulses with 100 μs pause as in our protocol 3. Similar experiments were performed by van Es et al. [12], who used a circular catheter with 14 electrodes to deliver monophasic 6 ms defibrillator pulses. Both arcing and gas release attributed to electrolysis were observed, however, their energies and total charge delivered were significantly higher than in our experiments.

Fig. 4 shows a low duty factor biphasic protocol (protocol 7) at elevated initial temperature. The longer train duration of this protocol resulted in more gradual heating. However, the numerical model still predicts that the temperature reaches the boiling point near the electrode edges. This sequence shows a much larger number of bubbles with a larger volume. Based on the bubble diameter measurements in frame 6 (Fig. 4), we estimate the total volume of bubbles to be about 1.5 μl. Although we cannot distinguish between the degassing effect due to local heating and boiling of the water near the electrode edges, the maximum volume of gas released due to solubility reduction reported in Table 2 is an order of magnitude smaller than the bubbles we observe on camera. Therefore, we attribute most of these bubbles to boiling and resulting steam formation. The video also shows that only a few very small bubbles detach from the electrode edges and drift away from the catheter, which is consistent with bubble loop experiments (see continuation).

Fig. 5 shows protocol 4 with 2–2–2–2 pulses, resulting in a duty cycle

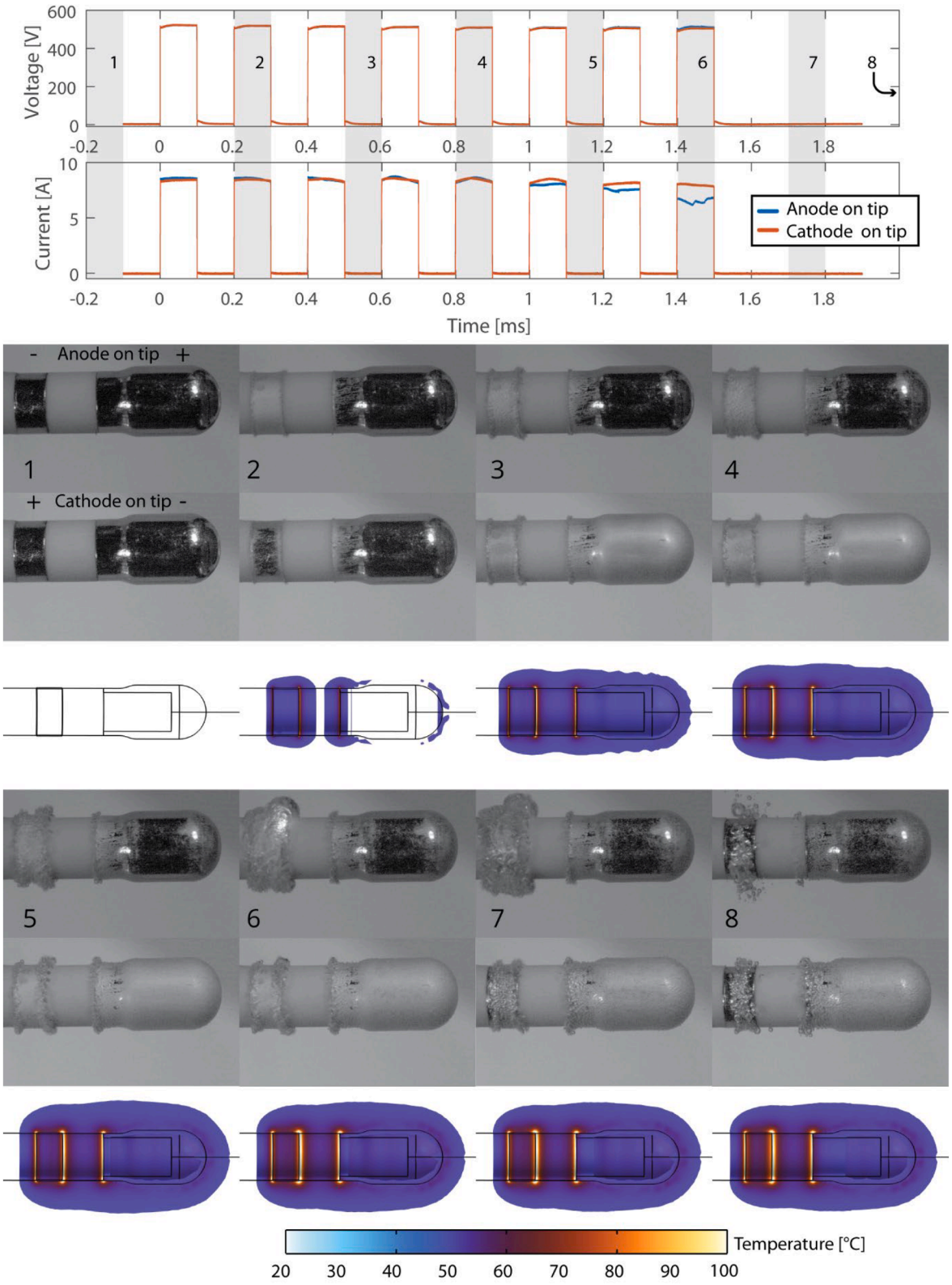

Fig. 3. Delivery of fast monophasic (protocols 3 and 4, 100–100 and reversed 100–100) pulses between the catheter tip and ring electrodes. Initial temperature in the experiment was 56.5 °C. The oscilloscope recordings of pulses are shown on top. The duration of exposure of each movie frame is indicated by the grey-shaded area. The stills from the high-speed recording are below, with the number corresponding to the time point indicated on the pulse train. The images are shown in three rows, with the first row showing anode at tip, second row showing cathode on tip, and the third row showing the numerical simulation of temperature rise during the pulse train. The numerical simulation only shows areas with a temperature increase of at least 1 °C. Note that there are two additional proximal ring electrodes, which are further away from the catheter tip and were not imaged.

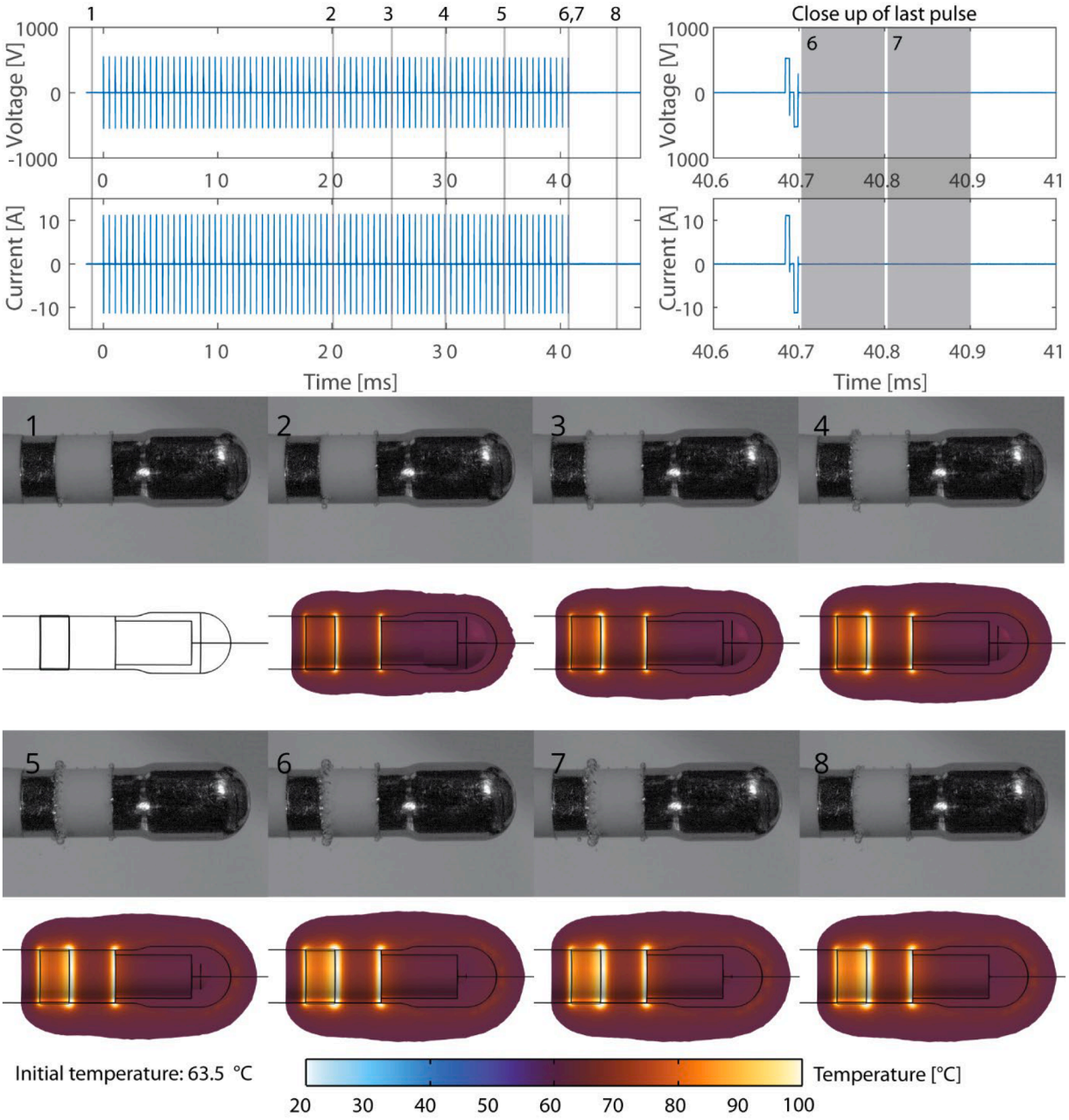

Fig. 4. Low duty factor biphasic protocol (5–5–5–500) at elevated temperature. Initial temperature was 63.5 °C. The selection of stills shows different time points during the pulse train at time points indicated on the oscilloscope recording. The numerical simulation only shows areas with a temperature increase of at least 1 °C.

of 0.5. This results in rapid heating of the fluid around the electrode edges, which occurs with similar dynamics to the fast 100 μs protocol. Bubbles are clearly visible at the electrode edges (approximately 3.3 μl), which can be attributed to boiling as suggested by simulations. The first time points when bubbles can clearly be seen is the second frame in Fig. 5, acquired between 402 and 500 μs after the first pulse. The biphasic protocol prevents the electrochemical products of hydrolysis from forming bubbles, even though the total charge transfer and therefore intensity of electrochemical reactions are very similar.

For biphasic pulses and the employed geometry, the dominant mechanism of bubble formation in the used protocols is boiling. While numerical simulations show that degassing could result in measurable volumes of air, this accounts for only a small portion of the total observed volume. Additionally, since no bubbles are seen before the numerical model predicts temperatures of 100 °C, the initial observed bubbles can be attributed to boiling. Degassing would already occur in the temperature range between 70 and 90 °C, which coincides with the lowest solubility of oxygen and nitrogen. However, since the volume fraction of gas solubility is less than 0.02, for bubbles to form by this mechanism, there would need to be convection of liquid bringing more gas to the nucleation sites, but this movement on timescales of the pulse delivery is negligible [33]. Although these conclusions appear to contradict those published by Verma et al. [39] using a different pulse generator to deliver pulses to *in vivo* thigh muscles, the location of the temperature probe used in their study was possibly some distance away from the hotspot. At a similar location to theirs, our modelling shows temperature rises of approximately 5 °C, similar to the values they have reported for the lowest energy setting. Although the treatment protocol was not disclosed, the total treatment time at this setting is most comparable to the results herein. This also illustrates that point temperature measurements are potentially misleading, as hot spots may be located elsewhere.

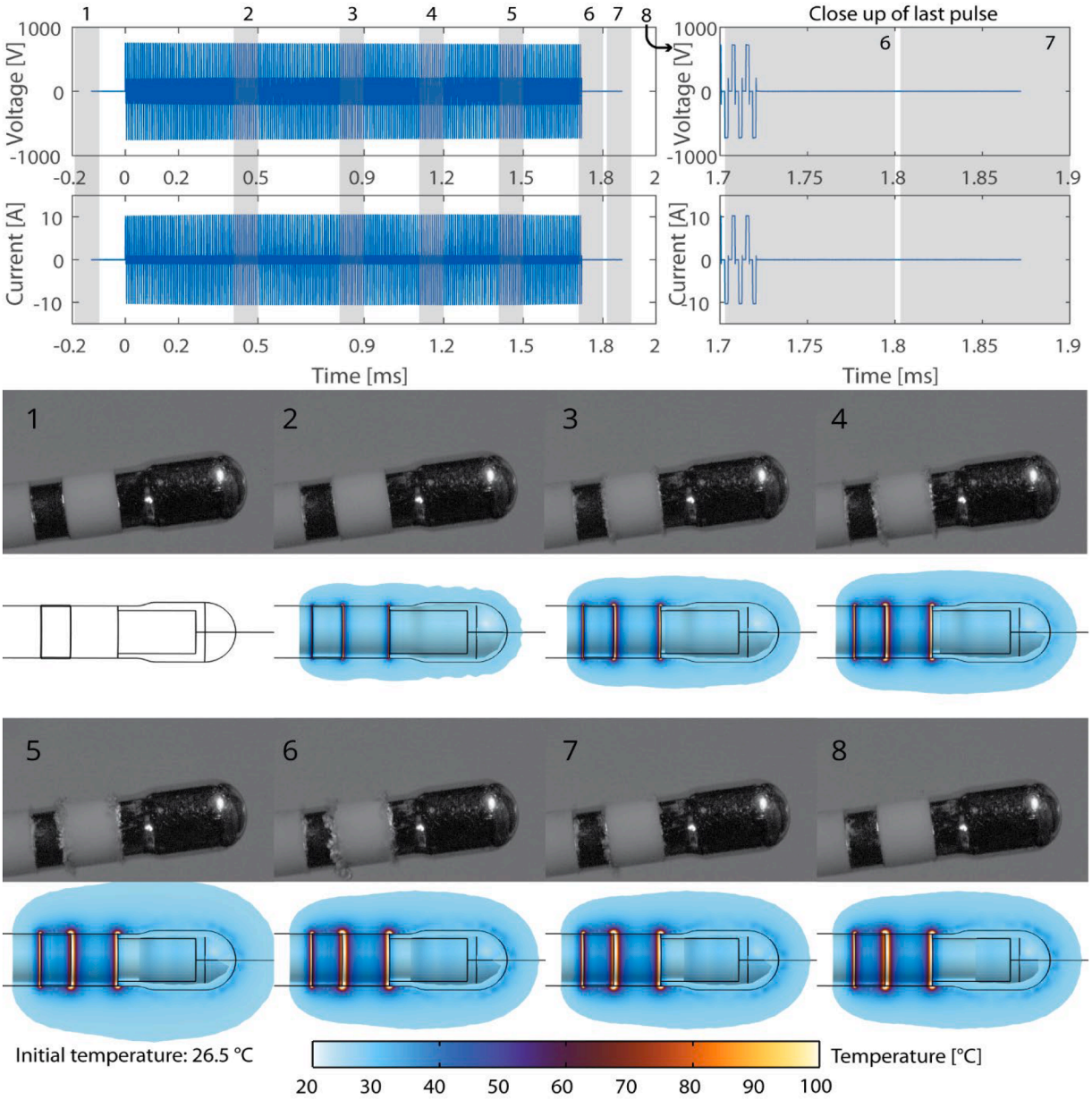

Fig. 5. High duty factor biphasic protocol at room temperature. The initial temperature of the experiment was 26.5 °C. The selection of stills shows different time points during the pulse train. The numerical simulation only shows areas with a temperature increase of at least 1 °C. For comparison with a low duty factor biphasic protocol, see supplemental figure S3.

Our high-speed camera results align very well with the bubble loop experiments (Fig. 6). There is a significant difference between the monophasic and biphasic protocols ($p < 0.001$, Kruskal-Wallis). This confirms that there is a large number and considerable volume of persistent bubbles forming for monophasic protocols, which detach from the electrodes due to fluid flow and are detected by the counter. In contrast, in the biphasic protocols, there are significantly fewer bubbles with a smaller total volume. Fig. 6 also shows that most experiments exhibited a significant dependence of the volume and number of bubbles on the applied voltage ($p < 0.05$ on slope of linear regression using the model of the form $X = \beta_0 + \beta_1 V_{appl}$, where X is either volume or number of bubbles, β_0 is the intercept, β_1 is the slope, and V_{appl} is the voltage applied to the catheter).

The total volume of detected bubbles in protocol 5 (2–2–2–2) is close to the maximum volume of degassed air, as computed from simulations, where some discrepancies can be attributed to the relatively large fluid flow around the catheter of 1 l/min. This contributes to the advection of heat and consequently lower volume of degassing, since a larger volume of saline experiences a lower temperature rise. This effect is more pronounced in longer pulse protocols (e.g., 6, 7), than in the short protocols (e.g. 5). The results combined with the high-speed video evidence indicate that the bubbles detectable using a bubble loop are most likely the result of electrolysis and degassing, since any steam bubbles will quickly condense back into the liquid phase. If electrolysis is eliminated, the only long-lived bubbles which can result from PFA are likely to be due to degassing of the liquid. Since water vapour is so short lived, it is more likely that any thromboembolic pathological findings in end organs such as the kidney, if they are caused by air embolism, are likely due to air bubbles with longer half-lives in the blood. We speculate that bubbles formed due to degassing of the medium, but also bubbles that have been formed due to air ingress into the body (typical air embolism), are more likely to cause such peripheral embolic events than water vapour. More research is needed to confirm this hypothesis.

Although the conclusion that most of the bubbles seen in high speed

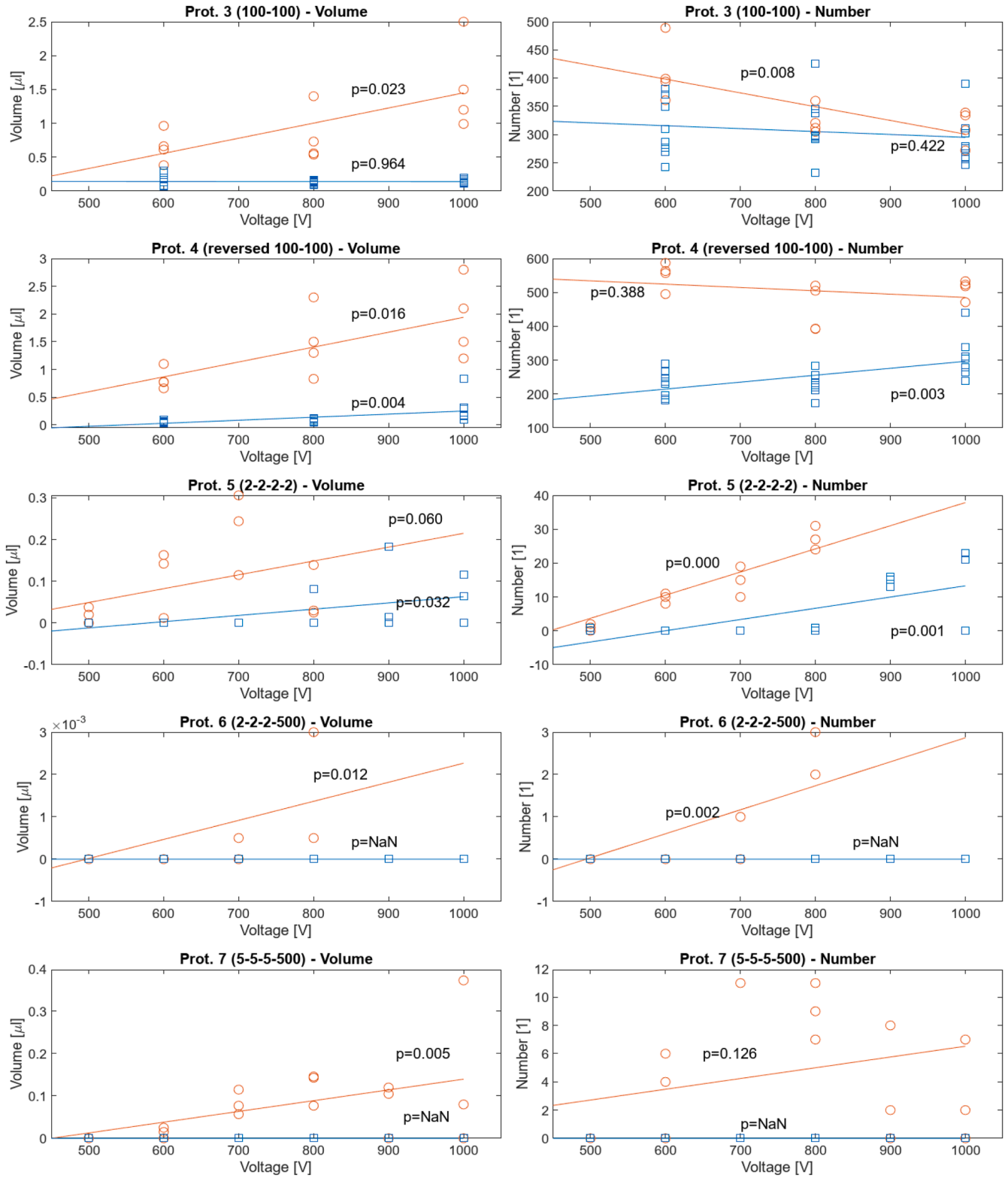

Fig. 6. Results of the bubble loop experiments. Each protocol is plotted for the room temperature (blue) and elevated temperature (red). Lines indicate linear model fit of the form $y = k \cdot y + c$. The indicated p values show the significance of the slope coefficient (k) of the linear model. Blue rectangles indicate measured data points at room temperature, while the red circles indicate the measured data points at 60 °C.

video experiments are due to boiling seems to contradict the findings of previous PFA studies [3], the authors of that study considered only the possibility of degassing and hydrolysis. Since the waveforms of those experiments are not disclosed it is challenging to find the reason for this discrepancy. However, it is important to note, that their experiments were done in vivo, therefore in blood, and with flow. A more relevant comparison is therefore with the bubble loop experiments, where e.g. protocol 5 already shows bubbles at room temperature, which we attribute at least partly to degassing.

Our study comes with limitations. First, in practical applications of

cardiac ablation, blood is much more complex than saline, which means that the volumes of gas formation in saline are likely to be different from that in blood. Second, blood plasma has a high protein concentration, which could affect the process of bubble formation and their persistence. In addition, the localized hotspots and rapid heating to temperatures near or above 100 °C could cause protein denaturation by a process whose temporal dynamics are poorly understood (thresholds for protein coagulation are from 85 to 98 °C after irradiation with millisecond laser pulses [40]), with unknown effects on bubble formation.

4. Conclusions

Our study found that bubbles originating from electrochemical reactions are more prevalent in monophasic pulsing protocols, whereas in high frequency biphasic pulsing protocols the bubbles are mainly caused by boiling of the medium. Degassing of liquid due to lower solubility of gasses at elevated temperatures plays a role, though a minor one. We also observed that bubbles caused by boiling collapse rapidly, whereas electrochemically produced bubbles and those produced through degassing appear to have longer lifetimes.

Therefore, to avoid or minimize potential bubble formation in intracardiac electroporation therapies such as pulsed field ablation, our study indicates it is of crucial importance to consider: i.) the choice of the treatment protocol used to deliver the energy, in particular with respect to mono- vs. biphasic delivery; ii.) an appropriate choice of the treatment protocol duty cycle and power, considering the thermal relations near the electrodes to avoid excessive heating of the medium due to excessive power; and iii.) design of applicator/electrode geometry with consideration of the local current density to avoid thermal hotspots.

Specifically, the data from our experiments supports the use of biphasic waveforms with individual pulse phase lengths short enough to not yet result in faradaic currents that would be leading to electrochemical production of bubbles. The current in this case would be confined to charging and discharging the double layer capacitance at the electrodes continuously. The duty cycle of such biphasic protocols will have to be a delicate balance between protocol efficiency (in terms of cell damage/kill) and heat production/dissipation, a balance which should be determined based on numerically or experimentally supported optimisation. As for the applicator/electrode geometry, our study shows that sharp edges are to be avoided, if possible, especially if they are at proximity anode-to-cathode as this carries the potential of facilitating arcing.

CRediT authorship contribution statement

Samo Mahnič-Kalamiza: Investigation, Methodology, Formal analysis, Visualization, Writing – original draft, Writing – review & editing. **Damijan Miklavčič:** Conceptualization, Visualization, Writing – review & editing, Supervision. **Peter Lombergar:** Methodology, Formal analysis, Writing – original draft, Writing – review & editing. **Blaž Mikuž:** Investigation, Writing – review & editing. **Lars M. Mattison:** Investigation, Methodology, Writing – review & editing. **Daniel C. Sigg:** Investigation, Methodology, Writing – review & editing. **Bor Kos:** Investigation, Methodology, Formal analysis, Visualization, Writing – original draft, Writing – review & editing.

Declaration of competing interest

The authors declare the following financial interests/personal relationships which may be considered as potential competing interests: Damijan Miklavcic reports financial support was provided by Medtronic. Bor Kos reports financial support was provided by Medtronic. Lars M Mattison reports a relationship with Medtronic that includes: employment. Daniel C Sigg reports a relationship with Medtronic that includes: employment. If there are other authors, they declare that they have no known competing financial interests or personal relationships that could have appeared to influence the work reported in this paper.

Data availability

Data is shared in a repository for review and will be published upon acceptance.

Acknowledgements

The study was partially funded by Medtronic. Authors acknowledge support of the Slovenian Research Agency (ARIS); grants P2-0249 and P2-0026 (high-speed camera acquisition at the Jožef Stefan Institute).

The authors also acknowledge fruitful discussions with Gonzalo Martinez (Medtronic) and colleagues Katja Balantič and Matej Reberšek (University of Ljubljana). During the preparation of this work the author (s) used InstaText.io in order to improve the clarity of the text and English grammar. After using this tool/service, the authors reviewed and edited the content as needed and take full responsibility for the content of the publication.

Supplementary materials

Supplementary material associated with this article can be found, in the online version, at doi:10.1016/j.electacta.2024.144550.

Original video files are available in the figshare repository at: https://doi.org/10.6084/m9.figshare.24433603.

Original cine files from high speed camera are available in the figshare repository at: https://doi.org/10.6084/m9.figshare.24081510.v1.

COMSOL Simulation files are available in the figshare repository at: https://doi.org/10.6084/m9.figshare.24434596.v1.

References

[1] M.B. Bendix, E. Brint, P.F. Forde, Electroporation of suspension cell lines – A proposed assay set for optimizations, Bioelectrochemistry 142 (2021) 107891, https://doi.org/10.1016/j.bioelechem.2021.107891.

[2] M. Punjiya, A. Mocker, B. Napier, A. Zeeshan, M. Gutsche, S. Sonkusale, CMOS microcavity arrays for single-cell electroporation and lysis, Biosens. Bioelectron. 150 (2020) 111931, https://doi.org/10.1016/j.bios.2019.111931.

[3] A. Verma, S.J. Asivatham, T. Deneke, Q. Castellvi, R.E. Neal, Primer on pulsed electrical field ablation, Circ.: Arrhythmia Electrophys. 14 (2021) e010086, https://doi.org/10.1161/CIRCEP.121.010086.

[4] M.C. Bonferoni, G. Rassu, E. Gavini, M. Sorrenti, L. Catenacci, M.L. Torre, S. Perteghella, L. Ansaloni, M. Maestri, P. Giunchedi, Electrochemotherapy of deep-seated tumors: state of art and perspectives as possible "EPR effect enhancer" to improve cancer nanomedicine efficacy, Cancers (Basel) 13 (2021) 4437, https://doi.org/10.3390/cancers13174437.

[5] L.G. Campana, I. Edhemovic, D. Soden, A.M. Perrone, M. Scarpa, L. Campanacci, M. Cemazar, S. Valpione, D. Miklavčič, S. Mocellin, E. Sieni, G. Sersa, Electrochemotherapy – emerging applications technical advances, new indications, combined approaches, and multi-institutional collaboration, Eur. J. Surg. Oncol. 45 (2019) 92–102, https://doi.org/10.1016/j.ejso.2018.11.023.

[6] N. Boc, I. Edhemovic, B. Kos, M.M. Music, E. Brecelj, B. Trotovsek, M. Bosnjak, M. Djokic, D. Miklavcic, M. Cemazar, G. Sersa, Ultrasonographic changes in the liver tumors as indicators of adequate tumor coverage with electric field for effective electrochemotherapy, Radiol. Oncol. 52 (2018) 383–391, https://doi.org/10.2478/raon-2018-0041.

[7] M. Brloznik, N. Boc, G. Sersa, J. Zmuc, G. Gasljevic, A. Seliskar, R. Dezman, I. Edhemovic, N. Milevoj, T. Plavec, V. Erjavec, D. Pavlin, M. Bosnjak, E. Brecelj, U. L. Tratar, B. Kos, J. Izlakar, M. Stukelj, D. Miklavcic, M. Cemazar, Radiological findings of porcine liver after electrochemotherapy with bleomycin, Radiol. Oncol. 53 (2019) 415–426, https://doi.org/10.2478/raon-2019-0049.

[8] K.N. Aycock, R.V. Davalos, Irreversible electroporation: background, theory, and review of recent developments in clinical oncology, Bioelectricity 1 (2019) 214–234, https://doi.org/10.1089/bioe.2019.0029.

[9] M.H.A. Groen, R. van Es, B.R. van Klarenbosch, M. Stehouwer, P. Loh, P. A. Doevendans, F.H. Wittkampf, K. Neven, In vivo analysis of the origin and characteristics of gaseous microemboli during catheter-mediated irreversible electroporation, EP Europace 23 (2021) 139–146, https://doi.org/10.1093/europace/euaa243.

[10] S. McBride, S. Avazzadeh, A.M. Wheatley, B. O'Brien, K. Coffey, A. Elahi, M. O'Halloran, L.R. Quinlan, Ablation modalities for therapeutic intervention in

arrhythmia-related cardiovascular disease: focus on electroporation, J. Clin. Med. 10 (2021) 2657, https://doi.org/10.3390/jcm10122657.
[11] K. Neven, A. Füting, I. Byrd, R.W. Heil, J.M. Fish, D.A. Feeney, E. Donskoy, J. A. Jensen, Absence of (sub-)acute cerebral events or lesions after electroporation ablation in the left-sided canine heart, Heart Rhythm 18 (2021) 1004–1011, https://doi.org/10.1016/j.hrthm.2021.02.015.
[12] R. Van Es, M.H.A. Groen, M. Stehouwer, P.A. Doevendans, F.H.M. Wittkampf, K. Neven, In vitro analysis of the origin and characteristics of gaseous microemboli during catheter electroporation ablation, Cardiovasc. Electrophysiol. 30 (2019) 2071–2079, https://doi.org/10.1111/jce.14091.
[13] E. Rowland, R. Foale, P. Nihoyannopoulos, M. Perelman, D.M. Krikler, Intracardiac contrast echoes during transvenous His bundle ablation, Br. Heart J. 53 (1985) 240–242.
[14] G.H. Bardy, F. Coltorti, T.D. Ivey, C. Alferness, M. Rackson, K. Hansen, R. Stewart, H.L. Greene, Some factors affecting bubble formation with catheter-mediated defibrillator pulses, Circulation 73 (1986) 525–538, https://doi.org/10.1161/01.cir.73.3.525.
[15] C. Herrera Siklódy, T. Deneke, M. Hocini, H. Lehrmann, D.-I. Shin, S. Miyazaki, S. Henschke, P. Fluegel, J. Schiebeling-Römer, P.M. Bansmann, T. Bourdias, V. Dousset, M. Haïssaguerre, T. Arentz, Incidence of asymptomatic intracranial embolic events after pulmonary vein isolation: comparison of different atrial fibrillation ablation technologies in a multicenter study, J. Am. Coll. Cardiol. 58 (2011) 681–688, https://doi.org/10.1016/j.jacc.2011.04.010.
[16] J. Herm, J.B. Fiebach, L. Koch, U.A. Kopp, C. Kunze, C. Wollboldt, P. Brunecker, H.-P. Schultheiss, A. Schirdewan, M. Endres, K.G. Haeusler, Neuropsychological effects of MRI-detected brain lesions after left atrial catheter ablation for atrial fibrillation: long-term results of the MACPAF study, Circ. Arrhythm. Electrophysiol. 6 (2013) 843–850, https://doi.org/10.1161/CIRCEP.113.000174.
[17] A. Kiss, E. Nagy-Baló, G. Sándorfi, I. Edes, Z. Csanádi, Cerebral microembolization during atrial fibrillation ablation: comparison of different single-shot ablation techniques, Int. J. Cardiol. 174 (2014) 276–281, https://doi.org/10.1016/j.ijcard.2014.03.175.
[18] A. Verma, D.E. Haines, L.V. Boersma, N. Sood, A. Natale, F.E. Marchlinski, H. Calkins, P. Sanders, D.L. Packer, K.-H. Kuck, G. Hindricks, B. Onal, J. Cerkvenik, H. Tada, D.B. DeLurgio, Pulsed Field Ablation for the Treatment of Atrial Fibrillation: PULSED AF Pivotal Trial, Circulation 147 (2023) 1422–1432, https://doi.org/10.1161/CIRCULATIONAHA.123.063988.
[19] V.Y. Reddy, E.P. Gerstenfeld, A. Natale, W. Whang, F.A. Cuoco, C. Patel, S. E. Mountantonakis, D.N. Gibson, J.D. Harding, C.R. Ellis, K.A. Ellenbogen, D. B. DeLurgio, J. Osorio, A.B. Achyutha, C.W. Schneider, A.S. Mugglin, E. M. Albrecht, K.M. Stein, J.W. Lehmann, M. Mansour, Pulsed field or conventional thermal ablation for paroxysmal atrial fibrillation, N. Engl. J. Med. 389 (2023) 1660–1671, https://doi.org/10.1056/NEJMoa2307291.
[20] A. Anić, T. Phlips, T. Brešković, P. Koopman, S. Girouard, V. Mediratta, Z. Jurišić, I. Sikirić, L. Lisica, J. Vijgen, Pulsed field ablation using focal contact force-sensing catheters for treatment of atrial fibrillation: acute and 90-day invasive remapping results, Europace 25 (2023) euad147, https://doi.org/10.1093/europace/euad147.
[21] H. Cindric, P. Mariappan, L. Beyer, P. Wiggermann, M. Moche, D. Miklavcic, B. Kos, Retrospective study for validation and improvement of numerical treatment planning of irreversible electroporation ablation for treatment of liver tumors, IEEE Trans. Biomed. Eng. 68 (2021) 3513–3524, https://doi.org/10.1109/TBME.2021.3075772.
[22] A. Zupanic, S. Ribaric, D. Miklavcic, Increasing the repetition frequency of electric pulse delivery reduces unpleasant sensations that occur in electrochemotherapy, Neoplasma 54 (2007) 246–250.
[23] T. Potočnik, D. Miklavčič, A. Maček Lebar, Gene transfer by electroporation with high frequency bipolar pulses in vitro, Bioelectrochemistry (2021) 107803, https://doi.org/10.1016/j.bioelechem.2021.107803.
[24] S. Mahnič-Kalamiza, D. Miklavčič, Scratching the electrode surface: insights into a high-voltage pulsed-field application from in vitro & in silico studies in indifferent fluid, Electrochim. Acta 363 (2020) 137187, https://doi.org/10.1016/j.electacta.2020.137187.
[25] R. van Es, M.K. Konings, B.C. Du Pré, K. Neven, H. van Wessel, V.J.H.M. van Driel, A.H. Westra, P.A.F. Doevendans, F.H.M. Wittkampf, High-frequency irreversible electroporation for cardiac ablation using an asymmetrical waveform, Biomed. Eng. Online 18 (2019) 75, https://doi.org/10.1186/s12938-019-0693-7.
[26] A. Vižintin, J. Vidmar, J. Ščančar, D. Miklavčič, Effect of interphase and interpulse delay in high-frequency irreversible electroporation pulses on cell survival, membrane permeabilization and electrode material release, Bioelectrochemistry 134 (2020) 107523, https://doi.org/10.1016/j.bioelechem.2020.107523.
[27] D.C. Sweeney, M. Reberšek, J. Dermol, L. Rems, D. Miklavčič, R.V. Davalos, Quantification of cell membrane permeability induced by monopolar and high-frequency bipolar bursts of electrical pulses, Biochim. Biophys. Acta (BBA) - Biomembr. 1858 (2016) 2689–2698, https://doi.org/10.1016/j.bbamem.2016.06.024.
[28] C.A. Schneider, W.S. Rasband, K.W. Eliceiri, NIH image to ImageJ: 25 years of image analysis, Nat. Methods 9 (2012) 671–675, https://doi.org/10.1038/nmeth.2089.
[29] P.A. Garcia, J.H. Rossmeisl Jr, R.E. Neal 2nd, T.L. Ellis, R.V. Davalos, A parametric study delineating irreversible electroporation from thermal damage based on a minimally invasive intracranial procedure, Biomed. Eng. Online 10 (2011) 34, https://doi.org/10.1186/1475-925X-10-34.
[30] R.B. McCleskey, Electrical conductivity of electrolytes found in natural waters from (5 to 90) °C, J. Chem. Eng. Data 56 (2011) 317–327, https://doi.org/10.1021/je101012n.
[31] G.D. Scott, D.M. Kilgour, The density of random close packing of spheres, J. Phys. D: Appl. Phys. 2 (1969) 863–866, https://doi.org/10.1088/0022-3727/2/6/311.
[32] R.T. Lahey, E. Baglietto, I.A. Bolotnov, Progress in multiphase computational fluid dynamics, Nucl. Eng. Design 374 (2021) 111018, https://doi.org/10.1016/j.nucengdes.2020.111018.
[33] R. Battino, T.R. Rettich, T. Tominaga, The solubility of nitrogen and air in liquids, J. Phys. Chem. Ref. Data 13 (1984) 563–600, https://doi.org/10.1063/1.555713.
[34] R. Battino, The Ostwald coefficient of gas solubility, Fluid Phase Equilib. 15 (1984) 231–240, https://doi.org/10.1016/0378-3812(84)87009-0.
[35] D.C. Sweeney, M. Reberšek, J. Dermol, L. Rems, D. Miklavčič, R.V. Davalos, Quantification of cell membrane permeability induced by monopolar and high-frequency bipolar bursts of electrical pulses, Biochim. Biophys. Acta 1858 (2016) 2689–2698, https://doi.org/10.1016/j.bbamem.2016.06.024.
[36] C. Yao, S. Dong, Y. Zhao, Y. Lv, H. Liu, L. Gong, J. Ma, H. Wang, Y. Sun, Bipolar microsecond pulses and insulated needle electrodes for reducing muscle contractions during irreversible electroporation, IEEE Transac. Biomed. Eng. 64 (2017) 2924–2937, https://doi.org/10.1109/TBME.2017.2690624.
[37] M. Scuderi, M. Rebersek, D. Miklavcic, J. Dermol-Cerne, The use of high-frequency short bipolar pulses in cisplatin electrochemotherapy in vitro, Radiol. Oncol. 53 (2019) 194–205, https://doi.org/10.2478/raon-2019-0025.
[38] B. Mercadal, N. Beitel-White, K.N. Aycock, Q. Castellví, R.V. Davalos, A. Ivorra, Dynamics of cell death after conventional IRE and H-FIRE treatments, Ann. Biomed. Eng. 48 (2020) 1451–1462, https://doi.org/10.1007/s10439-020-02462-8.
[39] A. Verma, P. Zhong, Q. Castellvi, S. Girouard, V. Mediratta, R.E. Neal, Thermal profiles for focal pulsed electric field ablation, JACC: Clin. Electrophys. (2023), https://doi.org/10.1016/j.jacep.2023.05.005. S2405500X23002888.
[40] T.J. Pfefer, B. Choi, G. Vargas, K.M. McNally, A.J. Welch, Pulsed laser-induced thermal damage in whole blood, J. Biomech. Eng. 122 (2000) 196–202, https://doi.org/10.1115/1.429642.